

# Direct numerical simulation of a compressible boundary-layer flow past an isolated three-dimensional hump in a high-speed subsonic regime

D. De Grazia,<sup>1,\*</sup> D. Moxey,<sup>2</sup> S. J. Sherwin,<sup>1</sup> M. A. Kravtsova,<sup>3</sup> and A. I. Ruban<sup>3</sup>

<sup>1</sup>*Department of Aeronautics, Imperial College London, London SW7 2AZ, United Kingdom*

<sup>2</sup>*College of Engineering, Mathematics and Physical Sciences, University of Exeter, Exeter EX4 4QF, United Kingdom*

<sup>3</sup>*Department of Mathematics, Imperial College London, London SW7 2AZ, United Kingdom*



(Received 15 June 2016; published 8 February 2018)

In this paper we study the boundary-layer separation produced in a high-speed subsonic boundary layer by a small wall roughness. Specifically, we present a direct numerical simulation (DNS) of a two-dimensional boundary-layer flow over a flat plate encountering a three-dimensional Gaussian-shaped hump. This work was motivated by the lack of DNS data of boundary-layer flows past roughness elements in a similar regime which is typical of civil aviation. The Mach and Reynolds numbers are chosen to be relevant for aeronautical applications when considering small imperfections at the leading edge of wings. We analyze different heights of the hump: The smaller heights result in a weakly nonlinear regime, while the larger result in a fully nonlinear regime with an increasing laminar separation bubble arising downstream of the roughness element and the formation of a pair of streamwise counterrotating vortices which appear to support themselves.

DOI: [10.1103/PhysRevFluids.3.024101](https://doi.org/10.1103/PhysRevFluids.3.024101)

## I. INTRODUCTION

Modern theory of separation of a fluid flow over a surface relies on an asymptotic analysis of the Navier-Stokes equations at large Reynolds numbers. The basic idea of this method belongs to Prandtl, who first used it in its classical study on boundary layers [1]. The boundary-layer theory, intended by Prandtl for predicting flow separation, was based on the so-called hierarchical approach where the outer inviscid flow is calculated first, ignoring the existence of the viscous region, and only after that one can study the boundary layer.

A key element of the separation process, which was not fully appreciated in Prandtl's theory, is a mutual interaction between the boundary layer and the external inviscid flow. Nevertheless, Prandtl's idea of subdividing the entire flow field in different regions is the basis of one of the most powerful tools in modern asymptotic analysis, the method of matched asymptotic expansions. The asymptotic theory of the viscous-inviscid interaction is known as triple-deck theory and was specifically designed with the purpose of describing the phenomenon of the boundary-layer separation at large values of the Reynolds number. The theory was formulated in [2,3] for the self-induced separation in supersonic flow and in [4,5] for incompressible fluid flows near the trailing edge of a flat plate. Later it became clear that the viscous-inviscid interaction plays a key role in many fluid flows. For a detailed description of the theory the interested reader can refer to [6].

In recent years a number of experimental and computational studies have been focused on the interaction between boundary-layer flows (both internal and external) and a small wall roughness, a hump, or an indentation. In [7] the authors analyzed the flow structure generated by a shallow

\*d.de-grazia12@imperial.ac.uk

three-dimensional hump in a two-dimensional boundary layer by applying the three-dimensional counterpart of the classical triple-deck theory. The theory of [7] was then generalized in [8] to make it applicable to the atmospheric boundary layer over hills. In the atmospheric boundary layer the flow stratification is important and, if this is increased or the surface roughness is made smaller, in terms of height, than that assumed in [7], then the so-called compensation flow is realized. Applications of triple-deck theory to three-dimensional flows with compensation can be found in [9–11], where the authors found that there is a significant difference between three-dimensional boundary layers with compensation and two-dimensional boundary layers [12]. Comparison of the linear solution of two- and three-dimensional flows with compensation is shown in [13]. The boundary-layer interaction with small wall roughness was analyzed in [14], where the authors studied the compensation flow regime. In [15,16] the authors analyzed the perturbations produced in the two-dimensional boundary layer by a row of identical and equally spaced roughnesses placed in a straight line perpendicular to the oncoming flow. In [17] the two-dimensional boundary layer encountering a three-dimensional roughness was studied in the hypersonic flow regime. The results of the present work show that, for the same roughness height, the perturbations in transonic flow are stronger and display a wider spread in the spanwise direction showing a slower decay than that exhibited in the hypersonic case.

All of the work cited above is based on triple-deck theory and analytical solution of simplified equations. Because of their high computational cost, direct numerical simulations have not been widely used in studies concerning roughness-induced transition in high-speed flows. However, a significant improvement in numerical techniques for solving the Navier-Stokes equations and the fast expansion of computational resources have made direct numerical simulation (DNS) a real possibility. More recently, DNS has been used to simulate the effect of roughness elements on the high-speed boundary-layer transition. In [18] the authors studied the effect of two-dimensional localized roughness on boundary-layer instability in a supersonic flow at Mach 4.8. Similar studies and instability analyses were performed in [19–21]. In [22] the authors studied transition due to an isolated smooth bump at Mach 3.0 and 6.0. Similar studies, extending the range of flow conditions and roughness shape, can be found in [23,24]. In [25,26] a receptivity study at Mach 6.0 boundary-layer flow over a sharp-edged localized roughness element was performed, taking into consideration the effect of roughness height, type of imposed disturbance, and wall temperature. In [27] the instabilities in the wake behind a sharp-edged roughness element at Mach 2.5 were analyzed using direct numerical simulations, spatial bi-global stability analysis, and analysis of the three-dimensional parabolized stability equations. A similar study was performed in [28], where the authors extended the work in [27] to roughness elements with three-dimensional geometries of various type considering a hypersonic flow at Mach 6.0.

In [29] Schneider provided a review of the hypersonic flow over roughness elements. In this work the effects of roughness on hypersonic transition are reviewed, considering the physics of the process, known parametric effects, some of the common correlations, and a few case studies. In [30] a direct comparison of experimentally observed and computed instabilities due to a cylindrical roughness in a boundary layer at Mach 6 to identify the dominant mechanism for transition is presented.

All the numerical studies presented are concerned with a supersonic or hypersonic regime; we are unaware of any DNS results in the literature of flows past roughness elements in the high-speed subsonic regime which is typical of civil aviation. The aim of this paper is to start closing the gap between the DNS results in the high-speed subsonic regime and the data present in the literature for similar analyses in supersonic and hypersonic regimes. The DNS study is the three-dimensional extension of the work done by Mengaldo *et al.* in [31]. Specifically, we perform a DNS study of a two-dimensional boundary-layer flow over a flat plate encountering a three-dimensional Gaussian-shaped hump at  $\text{Ma} = 0.87$ . We consider different heights of the hump: The smaller heights result in a weakly nonlinear regime, while the larger result in a fully nonlinear regime with an increasing laminar separation bubble arising downstream of the roughness element. We found that, if the roughness height is small, then the perturbations decay rather fast everywhere except in the wake behind the roughness where they decay slowly. However, if the height is greater than some critical value, two symmetric vortices form in the wake and they appear to support themselves and grow with the distance

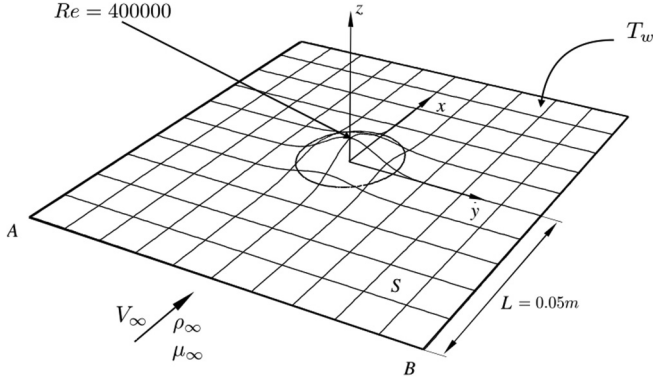


FIG. 1. Problem formulation. (Courtesy of [17].)

from the roughness. This growth is well described by the difference between the actual longitudinal velocity and its unperturbed value. This difference develops a distinctive minimum at some position above the wall. As the streamwise distance from the roughness increases, the minimum gets deeper and its position moves farther away from the wall.

In Sec. II we detail the model problem considered and in Sec. III we present the numerical techniques applied for the DNS. In Sec. IV we present the results and the main findings of our analysis detailing the effects of two- and three-dimensional geometries, Mach number, and roughness height. In Sec. V a summary and conclusions are outlined.

## II. PROBLEM FORMULATION

The problem considered consists of a two-dimensional high-speed subsonic flow of a perfect gas over a rigid flat surface encountering a small three-dimensional roughness located at a distance  $L$  from the leading edge  $AB$  (see Fig. 1). Our task is to analyze the disturbances produced in the flow by the interaction between the boundary layer and the roughness. The roughness shape is defined by the equation

$$f(x, y) = h_r e^{-[(x-L)^2+y^2]/\beta^2}, \quad (1)$$

where  $L$  is the distance from the leading edge of the flat plate to the center of the roughness element,  $\beta$  is a parameter which controls the size of the roughness element, and  $h_r$  is the height of the roughness. A positive value of  $h_r$  defines a hump, a negative indentation. The Reynolds number was set equal to  $4 \times 10^5$  for all the simulations performed and is defined as

$$\text{Re} = \frac{\rho_\infty U_\infty L}{\mu_\infty}, \quad (2)$$

where  $V_\infty$  is the free-stream velocity,  $\rho_\infty$  and  $\mu_\infty$  are the density and the dynamic viscosity of the fluid at free-stream condition, respectively, and  $L$  is the typical length scale of the oncoming boundary layer which defines the distance the boundary layer develops along the body surface before encountering the obstacle.

In this DNS study we consider a transonic condition with a Mach number  $\text{Ma}_\infty = 0.87$  typical of aeronautical applications. The physical parameters adopted for the free-stream conditions are reported in Table I. The free-stream pressure  $p_\infty$ , density  $\rho_\infty$ , dynamic viscosity  $\mu_\infty$ , and thermal conductivity  $k_\infty$  correspond to an altitude of 11 000 m above sea level and they are based on the International Standard Atmosphere. The free-stream velocity  $\mathbf{V}_\infty = [U_\infty, 0, 0]$  was chosen in such a way that it satisfied the Mach number and we applied isothermal boundary conditions using a

TABLE I. Free-stream physical parameters for the study with  $\text{Ma}_\infty = 0.87$ .

$\text{Ma}_\infty$	$\rho_\infty (\text{kg m}^{-3})$	$p_\infty (\text{Pa})$	$\mu_\infty (\text{Pa m})$	$k_\infty (\text{W m}^{-1} \text{K}^{-1})$	$U_\infty (\text{m s}^{-1})$	$T_w (\text{K})$	$\text{Pr}$
0.87	0.364	22600	$1.167 \times 10^{-5}$	0.01629	256.5	258.0	0.72

temperature  $T_w$  at the wall. The temperature  $T_w$  was obtained through the Crocco integral defined as

$$c_P T_w = V_\infty^2 \left( \frac{1}{2} + \frac{1}{(\gamma - 1) \text{Ma}_\infty^2} \right). \quad (3)$$

Even if this could be deemed as not being the best and most usual practice for calculating the surface temperature, the value obtained through the Crocco integral is only slightly warmer than that calculated, for example, with a reasonable recovery factor. Moreover, it is a good approximation of the skin temperature close to the leading edge of civil aircraft at similar altitudes and speeds. In addition, this choice permitted a direct comparison of the results with those obtained for the equivalent two-dimensional simulations in [31,32]. The Prandtl number  $\text{Pr}$ , defined as the ratio of kinematic viscosity  $\nu$  to thermal diffusivity  $\alpha = k/\rho C_p$ , that is,  $\text{Pr} = C_p \mu/k$ , where  $C_p$  is the specific heat at constant pressure, was fixed and corresponds to the value commonly adopted for air. The length  $L = 0.05$  m for all the simulations performed.

We used different roughness heights, in order to investigate both weakly nonlinear and nonlinear regimes. The parameters adopted for the shape (i.e.,  $\beta$ ) and the height (i.e.,  $h_r$ ) of the humps are reported in Table II, along with the hump horizontal sizes  $\ell_{x,999} = \ell_{y,999}$ , which are defined as the length for which the ratio  $h(x)/h_r$  becomes smaller than 0.1%. In addition, we also report the values of the Mach number  $\text{Ma}_r$  calculated at  $[x, y, z] = [L - \ell_{x,999}/2, 0, h_r]$  and the corresponding Reynolds number based on the roughness height  $\text{Re}_r$  calculated as follows:

$$\text{Re}_r = \frac{\rho_r u_r h_r}{\mu_r}, \quad (4)$$

where  $\rho_r$ ,  $u_r$ , and  $\mu_r$  are the density, streamwise velocity, and dynamic viscosity at the location defined above.

The values of the second column in Table III correspond to the percentages with respect to the thickness of the compressible boundary layer at that location at Mach 0.87. This thickness is defined as the distance from the wall to the point where the velocity is 99% of the free-stream velocity. The boundary layer thickness at the hump location is  $4.9744 \times 10^{-4}$  m. The values in the third and fourth columns of Table III represent the percentages of the hump height with respect to its length and width. The free-stream parameters ( $\text{Ma}$ ,  $\text{Re}$ , and  $\text{Pr}$ ) were chosen to be relevant for aeronautical applications. The shape and the related parameters can be seen as simple models of small imperfections at the leading edge of civil aircraft wings.

In addition, the hump heights explored range from a nonseparated flow to a well-established separation bubble behind the obstacle. In particular, the maximum height explored can be considered small. This was chosen in order to study a pretransitional regime which can be compared with

TABLE II. Quantities relative to the different humps for the study with  $\text{Ma}_\infty = 0.87$ .

Hump	$h_r (\text{m})$	$\beta (\text{m})$	$\ell_{x,999} (\text{m})$	$\ell_{y,999} (\text{m})$	$\text{Ma}_r$	$\text{Re}_r$
$h_1$	$1 \times 1.94 \times 10^{-5}$	$1.7961 \times 10^{-4}$	$9.60 \times 10^{-4}$	$9.60 \times 10^{-4}$	0.054	7.71
$h_2$	$2 \times 1.94 \times 10^{-5}$	$1.7961 \times 10^{-4}$	$9.60 \times 10^{-4}$	$9.60 \times 10^{-4}$	0.107	30.70
$h_3$	$3 \times 1.94 \times 10^{-5}$	$1.7961 \times 10^{-4}$	$9.60 \times 10^{-4}$	$9.60 \times 10^{-4}$	0.162	69.45
$h_4$	$4 \times 1.94 \times 10^{-5}$	$1.7961 \times 10^{-4}$	$9.60 \times 10^{-4}$	$9.60 \times 10^{-4}$	0.213	122.00
$h_5$	$5 \times 1.94 \times 10^{-5}$	$1.7961 \times 10^{-4}$	$9.60 \times 10^{-4}$	$9.60 \times 10^{-4}$	0.265	191.4
$h_6$	$6 \times 1.94 \times 10^{-5}$	$1.7961 \times 10^{-4}$	$9.60 \times 10^{-4}$	$9.60 \times 10^{-4}$	0.323	276.9

TABLE III. Hump dimensions for the study with  $\text{Ma}_\infty = 0.87$ .

Hump	$h_r/\delta$ (%)	$h_r/\ell_{x,999}$ (%)	$h_r/\ell_{y,999}$ (%)
$h_1$	3.90	2.02	2.02
$h_2$	7.80	4.04	4.04
$h_3$	11.70	6.06	6.06
$h_4$	15.60	8.08	8.08
$h_5$	19.50	10.10	10.10
$h_6$	23.40	12.12	12.12

asymptotic results. In addition, the height of imperfections, such as rivets, present on the leading edge of civil aircraft, normalized with respect to the boundary-layer thickness, is even smaller and therefore, for the purpose of this work, there was no need to further increase the height.

In the following sections we will perform a comparison of the transonic regime with  $\text{Ma}_\infty = 0.87$  with a subsonic case with  $\text{Ma}_\infty = 0.5$  to show the influence of the Mach number. For a clearer presentation of the results we report here the correspondent tables for the subsonic case (see Tables IV–VI).

The boundary-layer thickness at the hump location is  $4.6190 \times 10^{-4}$  m. Note that the hump heights do not change between the transonic and subsonic cases. These correspond to 5%, 10%, 15%, 20%, 25%, and 30% of the thickness of an incompressible boundary layer.

### III. NUMERICAL APPROACH

In this section we present the numerical setup for the DNS of the boundary-layer flow past a roughness element.

#### A. The DNS domain and boundary conditions

The governing equations considered for the direct numerical simulations are the unsteady three-dimensional compressible Navier-Stokes equations. We use the explicit-in-time compressible aerodynamic solver included in the spectral-*hp* framework Nektar++ for our simulations, which is described in more detail in [33,34]. The spatial numerical discretization of the advection operator used is a collocation form of the discontinuous Galerkin (DG) spectral element method with a lumped mass matrix (see [35,36]). The Courant-Friedrichs-Lowy limit of this method is less restrictive than that of DG schemes with an exact mass matrix of the type of [37]. This, together with the diagonal nature of the lumped mass matrix, permitted a consistent speed-up of the simulations.

Note that we used an “exact” Riemann solver to calculate the advective numerical fluxes at the element interfaces. For further details on the exact Riemann solver the interested reader can refer to [38]. The boundary conditions (BCs) are applied in a weak manner by modifying the state from which the numerical fluxes are calculated. In particular, for the advection terms of the compressible Navier-Stokes equations, the weak BCs are implemented by defining a left and a right state. The left state is the inner state extrapolated from the interior of the domain, while the right state is the outer (ghost) state modified by imposing the boundary conditions described below. These states define the Riemann problem at the boundary and a Riemann solver is used to calculate the boundary intercell advective numerical flux. Details on Riemann solvers and how they pertain to the imposition of boundary conditions can be found in [38,39].

TABLE IV. Free-stream physical parameters for the study with  $\text{Ma}_\infty = 0.5$ .

$\text{Ma}_\infty$	$\rho_\infty$ ( $\text{kg m}^{-3}$ )	$p_\infty$ (Pa)	$\mu_\infty$ ( $\text{Pa m}$ )	$k_\infty$ ( $\text{W m}^{-1} \text{K}^{-1}$ )	$U_\infty$ ( $\text{m s}^{-1}$ )	$T_w$ (K)	Pr
0.50	0.364	22600	$6.707 \times 10^{-6}$	0.00936	147.4	258.0	0.72

TABLE V. Quantities relative to the different humps for the study with  $\text{Ma}_\infty = 0.5$ .

Hump	$h_r$ (m)	$\beta$ (m)	$\ell_{x,999}$ (m)	$\ell_{y,999}$ (m)	$\text{Ma}_r$	$\text{Re}_r$
$h_1$	$1 \times 1.94 \times 10^{-5}$	$1.7961 \times 10^{-4}$	$9.60 \times 10^{-4}$	$9.60 \times 10^{-4}$	0.031	4.43
$h_2$	$2 \times 1.94 \times 10^{-5}$	$1.7961 \times 10^{-4}$	$9.60 \times 10^{-4}$	$9.60 \times 10^{-4}$	0.062	17.64
$h_3$	$3 \times 1.94 \times 10^{-5}$	$1.7961 \times 10^{-4}$	$9.60 \times 10^{-4}$	$9.60 \times 10^{-4}$	0.093	39.91
$h_4$	$4 \times 1.94 \times 10^{-5}$	$1.7961 \times 10^{-4}$	$9.60 \times 10^{-4}$	$9.60 \times 10^{-4}$	0.124	70.12
$h_5$	$5 \times 1.94 \times 10^{-5}$	$1.7961 \times 10^{-4}$	$9.60 \times 10^{-4}$	$9.60 \times 10^{-4}$	0.155	110.00
$h_6$	$6 \times 1.94 \times 10^{-5}$	$1.7961 \times 10^{-4}$	$9.60 \times 10^{-4}$	$9.60 \times 10^{-4}$	0.186	159.14

The diffusion terms are discretized with the local discontinuous Galerkin (LDG) approach. For these terms the BCs are applied in a weak manner directly calculating the numerical flux at the given boundary by using a prescribed known solution (state). For further details on the LDG approach one can refer to [40].

Figure 2 shows a cross section of the domain of the simulations. We imposed the following boundary conditions: the inflow boundary condition (Inflow), the pressure outflow boundary condition (Outflow), the far-field boundary condition (Top), and the no-slip isothermal wall (Wall). At the subsonic inflow, where the viscous effects are not negligible, we need four physical boundary conditions. Specifically, we used a compressible flat-plate solution, obtained through an approximate similarity solution that will be described in the following section, for the density and the three velocity components, while the pressure is extrapolated from the interior of the domain. At the top boundary, where the viscous effects can be neglected, we impose all the variables via the similarity solution. The well-posedness of the BC is guaranteed by the use of the Riemann solver which takes into account the characteristics of the flow. For the subsonic outflow boundary we need one physical boundary condition. The pressure value is derived from the similarity solution, while all the other variables (density and velocity components) are extrapolated from the interior of the domain. For the no-slip isothermal wall the temperature imposed is obtained through the Crocco integral and the density is extrapolated from the interior of the domain. In the spanwise direction we applied periodic boundary conditions.

To initialize the simulation, the similarity solution was evaluated on a standard flat-plate domain without the Gaussian hump and then interpolated onto the domain with the hump. Although the initial boundary layer solution will deviate significantly from the flow at a later time in a large part of the domain (e.g., when separation occurs), this approximation of the initial flow shortens the route to steady-state convergence.

The computational domain is a Cartesian box extending for  $L_x \approx 40\delta$ ,  $L_y \approx 20\delta$ , and  $L_z \approx 6\delta$  in the streamwise ( $x$ ), spanwise ( $y$ ), and normal ( $z$ ) directions, where  $\delta$  is the compressible boundary-layer thickness at the roughness location at  $\text{Ma} = 0.87$  chosen as the reference length of the domain. The size of the domain in the streamwise direction was based on a sensitivity study performed in [31] for a similar two-dimensional problem. The size of the domain in the spanwise direction was based on considerations of the dimensions of flow structures behind the hump. In particular, in [17] it was observed that the vortices which form behind a roughness element decay rather fast with the distance

TABLE VI. Hump dimensions for the study with  $\text{Ma}_\infty = 0.5$ .

Hump	$h_r/\delta$ (%)	$h_r/\ell_{x,999}$ (%)	$h_r/\ell_{y,999}$ (%)
$h_1$	4.20	2.02	2.02
$h_2$	8.40	4.04	4.04
$h_3$	12.60	6.06	6.06
$h_4$	16.80	8.08	8.08
$h_5$	21.00	10.10	10.10
$h_6$	25.20	12.12	12.12

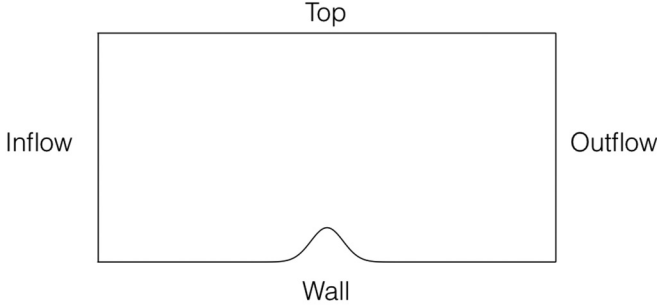


FIG. 2. The DNS domain and boundary conditions.

from the element in the spanwise direction, while they decay much more slowly in the streamwise direction. We therefore select a grid spacing in the spanwise direction that is half of the grid spacing in the streamwise direction. The wall-normal size used was based on consideration of the maximum hump height to simulate. In particular, the choice of the initial condition is not exactly representing the flow past the hump and this results in a transient following from the characteristic waves of the flow traveling in the domain. If there are any reflections arising from the choice of the boundary conditions, the wall-normal size of the domain guarantees that these reflections will not hit the wall for all the humps considered. This size satisfies the following rule typical of transonic flows:

$$L_z > \frac{\Delta x}{\sqrt{1 - Ma_\infty^2}}, \quad (5)$$

where  $\Delta x = \ell_{x,999}$  is the streamwise size of the roughness.

The final mesh adopted consisted of  $147 \times 36 \times 31$  elements in the streamwise, spanwise, and wall-normal directions, respectively, and is depicted in Figs. 3 and 4. In these figures  $\bar{x}$ ,  $\bar{y}$ , and  $\bar{z}$  are the nondimensional coordinates obtained dividing the dimensional coordinates  $x$ ,  $y$ , and  $z$  by the thickness of the undisturbed boundary layer at the hump location.

We performed a grid sensitivity study in order to assess the independence of the results from the resolution of the solution points. Specifically, we resolved the transonic 19.50% hump case with the mesh described using three different polynomial orders  $P = 2, 3, 4$ . The difference in terms of  $L^\infty$ -norm (normalized with respect to the respective absolute maximum values) between the finest resolution used and the coarsest was less than 1% for both the wall shear stress  $\tau_{xz}$  and the pressure gradient  $dp/dx$ . Details of the grid sensitivity study are depicted in Fig. 5. We note that, despite the presence of sharp features in these curves in the vicinity of the hump, the solutions obtained here are smooth and show no signs of oscillations or discontinuities between elements. We therefore conclude that the resolution chosen here is adequate for our study. We chose a polynomial order  $P = 3$  in each direction, therefore obtaining 588 solution points in the streamwise direction, 124 in the wall-normal direction, and 144 in the spanwise direction. A stretching technique was used in the wall-normal direction to better capture the boundary layer. The minimum  $\Delta z$  in proximity to the wall was equal to  $2 \times 10^{-6}$  m, which corresponds approximately to  $y^+ = 0.75$ . A nonuniform distribution in the streamwise and spanwise directions was also used to allow better resolution in the region close to the obstacle. In the streamwise direction the maximum resolution near the roughness element was equal to  $4 \times 10^{-6}$  m, which corresponds approximately to  $y^+ = 1.5$ , while in the spanwise direction it was equal to  $2 \times 10^{-5}$  m, which corresponds approximately to  $y^+ = 7.5$ . The description of the roughness element geometry was obtained using a fourth-order spline to achieve an accurate representation. For more details on the curvilinear boundary-layer mesh adopted one can refer to [41].

The polynomial order used was  $P = 3$  for all the simulations carried out and we applied a dealiasing technique (see [42]) when needed in order to avoid numerical instabilities in proximity

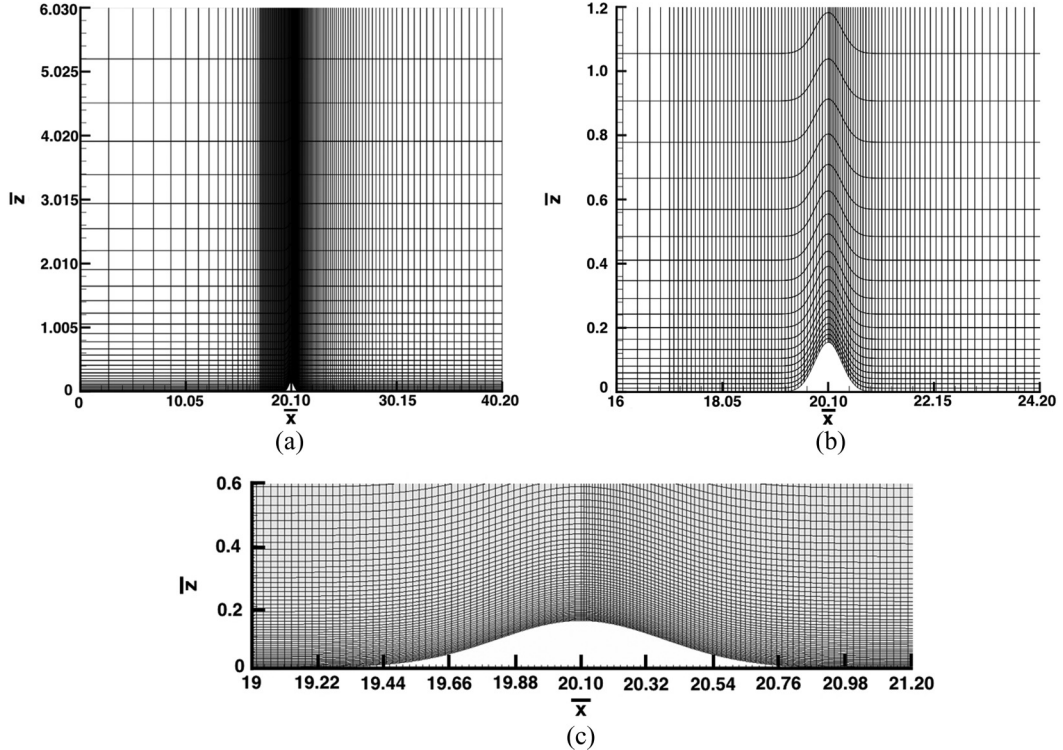


FIG. 3. Streamwise view of the mesh adopted for the DNS: (a) the entire mesh, (b) details of the mesh around the obstacle, and (c) resolution of the solution points around the hump.

of the hump location. The temporal discretization used was an explicit fourth-order Runge-Kutta scheme.

The simulations were run until convergence and the steady-state criterion adopted is the following:

$$\frac{\|g^t - g^{t+\Delta t}\|}{g_\infty} < 1 \times 10^{-8}, \quad (6)$$

where  $g$  is a conserved variable and  $g_\infty$  is the related free-stream value. The DNS process described made the simulations feasible in terms of computational costs and represents an efficient way for performing simulations on the configurations investigated.

### 1. Similarity solution

For compressible boundary-layer flow, an exact solution to the Navier-Stokes equations does not exist. However, it is possible to simulate the solution based on the boundary-layer approximation. In the present study of a two-dimensional compressible boundary layer developing over a flat surface encountering a roughness element, the Reynolds number is sufficiently high that a thin boundary layer will develop along the wall. The compressible boundary-layer equations can be used as initial conditions and as inflow conditions. Although the initial boundary-layer solution can deviate significantly from the flow at a later time in large parts of the flow domain (e.g., when separation occurs), it gives a good approximation to the solution at the inflow boundary, provided the flow is undisturbed in the inflow region. A correct inflow condition keeps the computational extent to a minimum, while a good approximation of the initial flow shortens the route to the (statistically) stationary state.

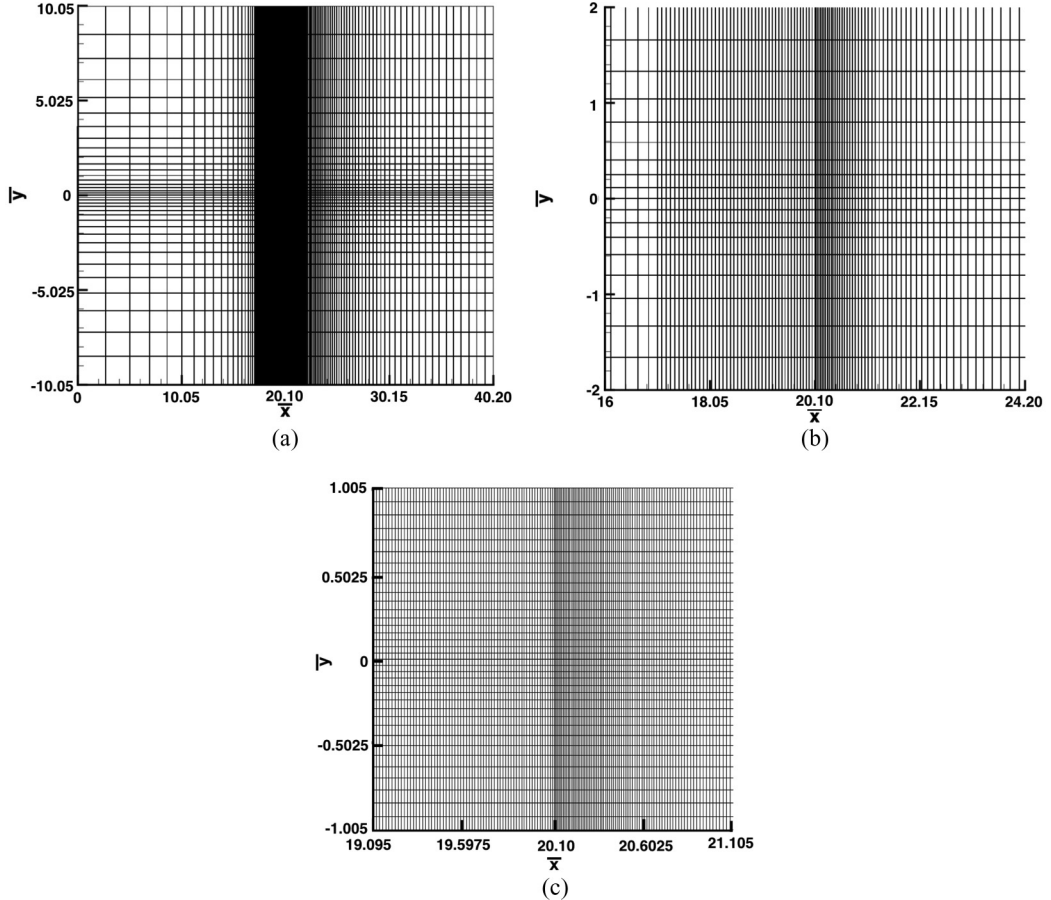


FIG. 4. Spanwise view of the mesh adopted for the DNS: (a) the entire mesh, (b) details of the mesh around the obstacle, and (c) resolution of the solution points around the hump.

Therefore, to save computational effort we use a velocity and temperature profile from a compressible similarity solution as the inlet and initial conditions for the computational domain. The similarity solution is obtained by reducing the compressible Navier-Stokes system of equations into the following system of two ordinary differential equations:

$$\begin{aligned} \frac{d}{d\eta} \left( \chi \frac{d^2 F}{d\eta^2} \right) + F \frac{d^2 F}{d\eta^2} &= 0, \\ \frac{d}{d\eta} \left( \frac{\chi}{Pr} \frac{dT'}{d\eta} \right) + F \frac{dT'}{d\eta} + (\gamma - 1) Ma^2 \chi \left( \frac{d^2 F}{d\eta^2} \right)^2 &= 0, \end{aligned} \quad (7)$$

with

$$u' = \frac{u}{U_\infty} = \frac{dF}{d\eta}, \quad T' = \frac{T}{T_\infty}, \quad \chi = \rho' \mu' = \frac{\rho \mu}{\rho_\infty \mu_\infty}, \quad (8)$$

where  $u$  and  $w$  are the velocity components in the streamwise and wall-normal directions, respectively, and  $T$  is the temperature. In this system  $F$  and  $T$  depend on the similarity variable

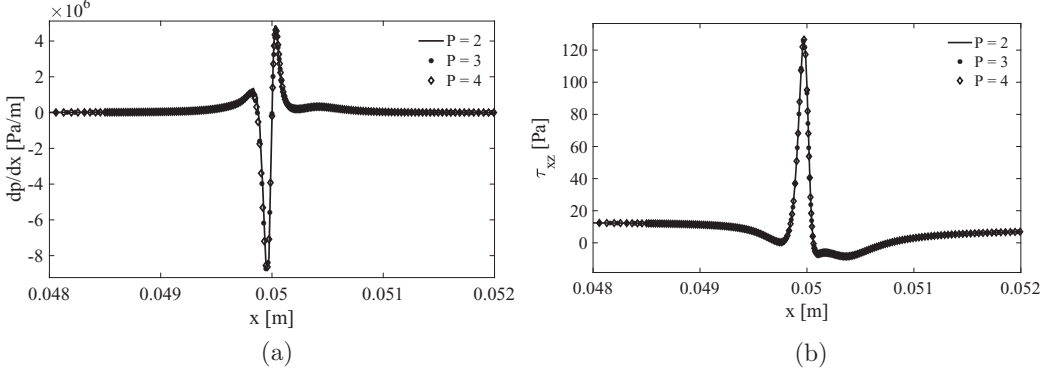


FIG. 5. Grid sensitivity analysis with polynomial orders  $P = 2, 3, 4$  for (a) the streamwise pressure derivative  $dp/dx$  and (b) the wall shear stress  $\tau_{xz}$ .

$\eta$  only, which is defined by the Dorodnitsyn-Stewartson transformation

$$\xi = x' = \frac{x}{L}, \quad \eta = \frac{1}{(2x')^{1/2}} \int_0^{z'} \rho'(x', s) ds = \left( \frac{\text{Re}}{2x} \right)^{1/2} \int_0^z \rho(x, s) ds, \quad (9)$$

with  $z' = \frac{\text{Re}^{1/2}}{L} z$ .

The following boundary conditions, which fully specify the similarity solution, are applied:

$$\frac{dF}{d\eta} \Big|_{z=0} = 0, \quad F|_{z=0} = 0, \quad \frac{dF}{d\eta} \Big|_{z \rightarrow \infty} = 1, \quad T'|_{z=0} = \frac{T_w}{T_\infty} T' \Big|_{z \rightarrow \infty} = 1. \quad (10)$$

For further details on the derivation of the system of the similarity solution the interested reader can refer to [43,44]. The solution to this system of equations can be used to reconstruct the desired flow field since use can be made of the relations  $u' = dF/d\eta$  and  $\rho' = 1/T'$  in view of the constant pressure in the boundary layer. This results in  $u'$ ,  $\rho'$ ,  $T'$ , and  $p'$ . The nondimensional vertical component of the velocity  $w'$  is then calculated by using the continuity equation. As a result, the field is now described as a function of  $\eta$  and we can then determine the dependence on the original coordinates  $x$  and  $z$ . To examine the performance of the similarity transformation, and therefore the quality of the initial condition, we compare the similarity solution of the compressible boundary-layer equations and a converged Navier-Stokes solution of a DNS of a flat plate with a leading edge. Specifically, we consider a flow over a flat plate at  $\text{Ma} = 0.87$  and  $\text{Re} = \rho_\infty U_\infty L / \mu_\infty = 4 \times 10^5$ , with  $L = 0.05$  m identical to that we aim to simulate.

The computational domain used is depicted in Fig. 6. At the inlet region, located at  $x = -0.15$  m, far-field boundary conditions were imposed, while at the outlet, located at  $x = 0.2$  m, pressure outflow boundary conditions were applied. In the region  $x \in [-0.15; 0.0]$  m,  $z = 0$  m, before the leading edge, symmetry boundary conditions were set, while in the region  $x \in [0.0; 0.2]$  m,  $z = 0$  m,

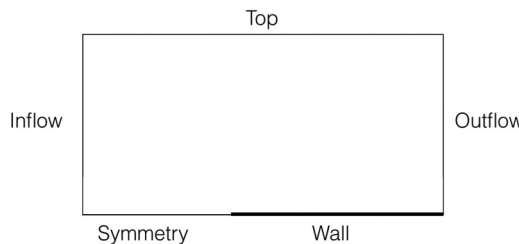


FIG. 6. The DNS domain of the flat-plate simulation and boundary conditions.

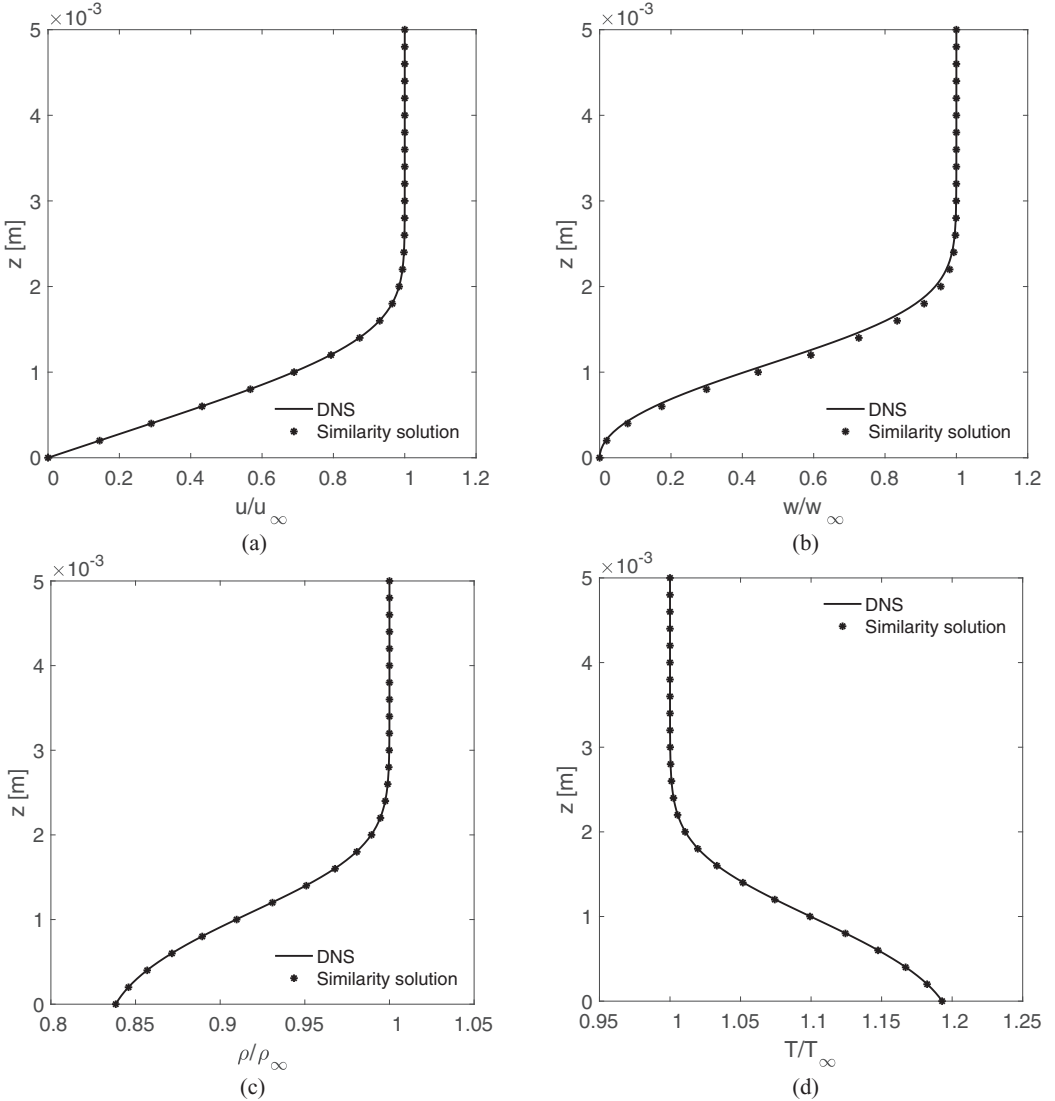


FIG. 7. (a) Streamwise velocity, (b) normal velocity components, (c) density, and (d) temperature at  $x = 0.05$  m, normalized by free-stream values, obtained from the similarity solution (closed circles) and Navier-Stokes computation (solid line).

isothermal no-slip boundary conditions were applied. Finally, at the top boundary, located at  $z \approx 100\delta$ , where  $\delta$  is the thickness of the boundary layer at the outlet, the far-field boundary conditions were used. Figure 7 shows the quantities normalized by their value at the edge of the boundary layer at  $x = L = 0.05$  m. We observe very good agreement between the similarity solution and the solution of Navier-Stokes equations.

#### IV. NUMERICAL RESULTS

In this section the DNS results of the boundary-layer flow studied are shown and analysed. We first present comparisons between two- and three-dimensional cases of different hump heights for  $\text{Ma}_\infty = 0.87$ . We then show a comparison between two different flow regimes: transonic with

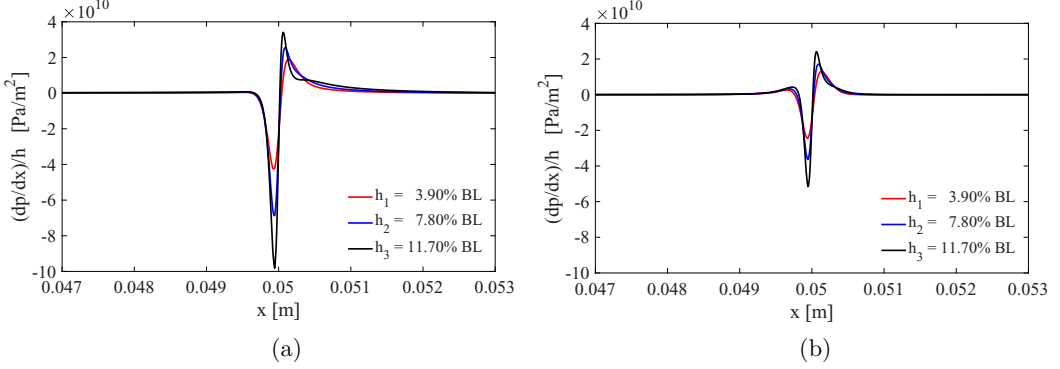


FIG. 8. Comparison of  $\frac{dp}{dx}$  normalized by hump height at the wall for the (a) two-dimensional and (b) three-dimensional cases, varying the hump heights.

$\text{Ma}_\infty = 0.87$  and subsonic with  $\text{Ma}_\infty = 0.5$ . Then we focus on the results of the three-dimensional hump case for the transonic regime in terms of wall shear stress, the shape of separation bubble, and streamwise vortices. We then explain the main findings of the study.

#### A. Two-dimensional vs three-dimensional geometry

In Figs. 8 and 9 we show the pressure derivative in the streamwise direction  $dp/dx$  normalized by hump height and the skin friction component  $\tau_{xz}$  at the wall for the three smallest hump heights studied in the transonic regime ( $\text{Ma}_\infty = 0.87$ ) for two- and three-dimensional cases. The three-dimensional results represent the flow quantities in the centerline of the domain.

We can see that the effects of the hump on the boundary-layer flow are larger in the two-dimensional case than in the three-dimensional case, in terms of both peaks and longitudinal extension of the perturbation. It is evident that, in order to produce the same perturbation effect of a two-dimensional hump, the equivalent three-dimensional hump must be higher. This trend was expected and can be explained with the smaller blockage effect that the flow around the three-dimensional shape encounters. In all the figures it is possible to see that the distortion of the boundary layer increases as the hump height increases. Specifically, in Fig. 8(a), we observe that the distortion of the normalized  $dp/dx$  behind the highest hump assumes a slightly different shape with a small change in curvature than the other humps. This indicates that, by increasing the hump height further, we may encounter the development of additional nonlinear effects which could potentially lead to the unsteadiness of

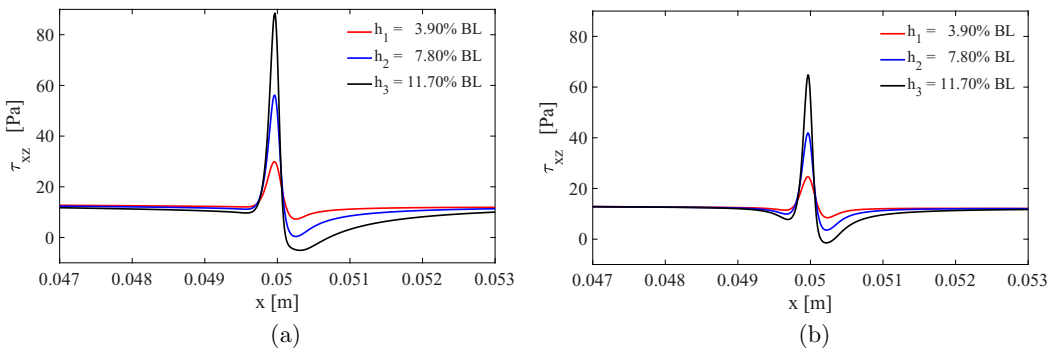


FIG. 9. Comparison of  $\tau_{xz}$  at the wall for the (a) two-dimensional and (b) three-dimensional cases, varying the hump heights.

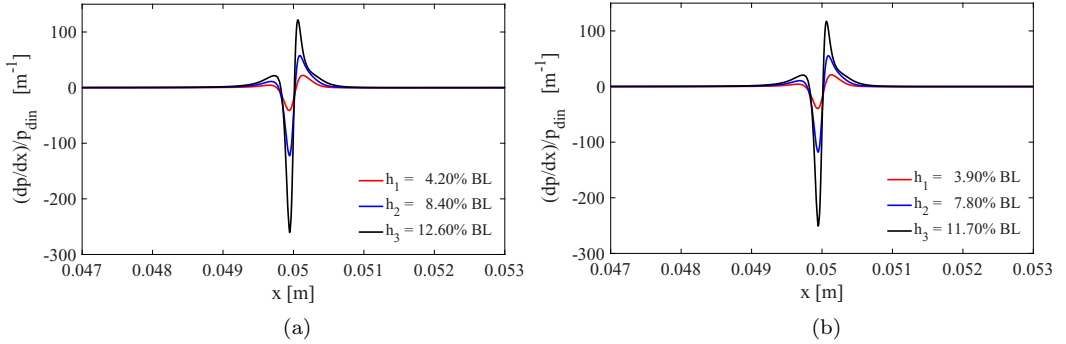


FIG. 10. Comparison of  $\frac{dp}{dx}$  normalized by free-stream dynamic pressure at the wall for (a)  $Ma_\infty = 0.50$  and (b)  $Ma_\infty = 0.87$ , varying the hump heights.

the separation bubble. It is likely that a similar shape will appear also for the three-dimensional case for a bigger hump height.

In Figs. 9(a) and 9(b) we see that the flow develops a small separation bubble behind the roughness element (the wall shear stress  $\tau_{xz}$  becomes negative in a small region behind the hump). We also note that the region of separated flow behind the hump is larger in the two-dimensional case than in three-dimensional case. It is also clear that the two-dimensional flow separates at a smaller height than the three-dimensional flow (note the differences in the minimum value of the 7.80% humps).

### B. Mach number effect

In Figs. 10 and 11 we show the pressure derivative in the streamwise direction  $dp/dx$  and the skin friction component  $\tau_{xz}$  at the wall for three smallest hump heights studied for two different flow regimes: subsonic with  $Ma_\infty = 0.5$  and transonic with  $Ma_\infty = 0.87$ . In order to compare the results of two different Mach numbers we normalized the pressure by free-stream dynamic pressure  $p_{din} = 0.5\rho_\infty U_\infty^2$  and the skin friction by the value of the skin friction  $\tau_{FP}$  at the hump location in the flat-plate simulation. These results represent the flow quantities at the centerline of the domain. In both figures we can see that the pressure gradient and the skin friction have a very similar behavior. As already mentioned, the distortion of the boundary-layer solution increases as the hump height increases for both parameters. Specifically, in Figs. 10(a) and 10(b) we also see that the behavior of the normalized  $dp/dx$  is very similar in terms of extension of the perturbation. The same comment

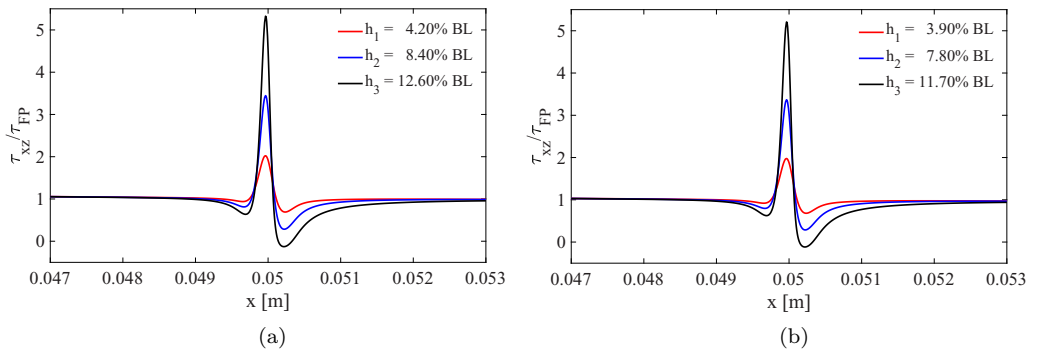


FIG. 11. Comparison of  $\tau_{xz}$  normalized by skin friction at the wall for (a)  $Ma_\infty = 0.50$  and (b)  $Ma_\infty = 0.87$ , varying the hump heights.

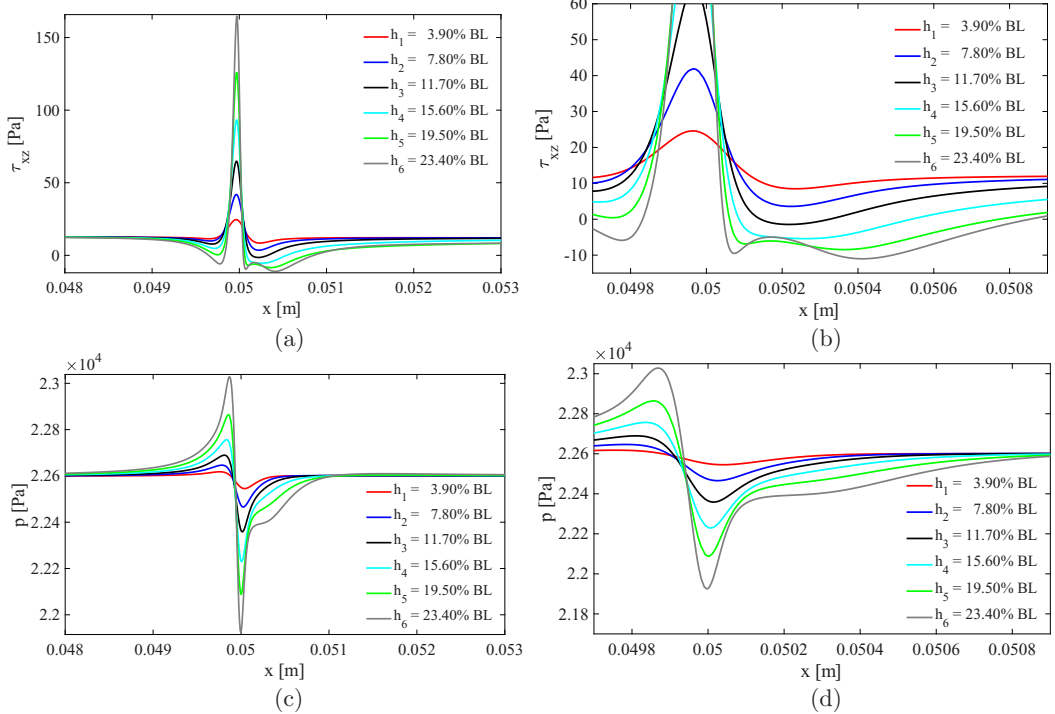


FIG. 12. Skin friction (a) and pressure (c) distribution along the centerline of the domain, varying the hump heights. Close-up around the hump location for skin friction (b) and pressure (d) distribution, respectively.

can be made of Figs. 11(a) and 11(b). In particular, the separation seems to appear at a similar hump height for both the subsonic and the transonic cases.

### C. Skin friction and pressure distributions

In Fig. 12 we show the distribution of  $\tau_{xz}$  and  $p$  at the wall in a plane along the centerline of the domain for the different hump heights simulated. We see that the perturbations increase as the hump height increases and we observe that, starting with the 11.70% hump, the flow develops a separation bubble behind the roughness. The extension of this separation region increases with the height of the hump.

In addition, we observe that the shape of the skin friction distribution behind the 19.50% hump is different from that of the humps with lower heights [see Fig. 12(b)] and this difference is even more evident with the 23.40% hump. In the region behind the hump, the pressure starts to rise, causing flow deceleration. The skin friction decreases, crossing zero at the separation point. It then reaches a minimum and starts to rise slowly. While it remains negative, the fluid in the separation region is moving in the opposite direction to the rest of the flow. The motion in this area is slow and for this reason the pressure develops a plateau, which can be clearly seen in Fig. 12(d). Then the skin friction starts to decrease again, reaching a second minimum, and further downstream it crosses zero at the reattachment point. Through the reattachment point the pressure monotonically increases and further downstream returns to its unperturbed value. Increasing the height of the hump, new features are likely to occur in the flow development like those seen in the analysis of the supersonic flow separation near a corner shown in [45]. In that study the authors observed the skin friction becoming positive again after the first minimum and after that a secondary region of separation inside the primary region before the second minimum.

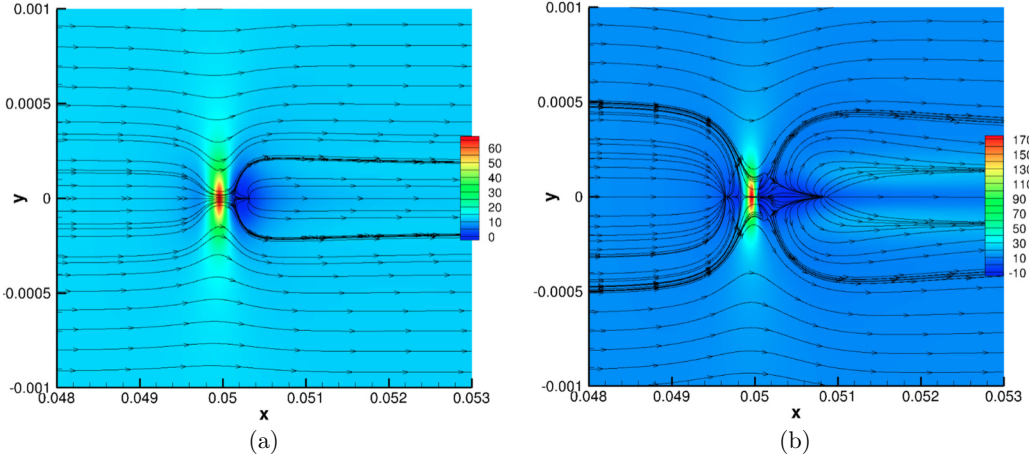


FIG. 13. Skin friction contours and limit streamlines at the wall, varying the hump heights: (a) 11.70% and (b) 23.40%.

In Figs. 12(a) and 12(b) we can also see that, when the hump becomes high enough, a small region of separation starts to develop before the roughness element, for example, in the 23.40% hump. This can be better appreciated in Fig. 13, where the contours of the skin friction at the wall are depicted for the 11.70% hump and the 23.40% hump. In both Figs. 13(a) and 13(b) we note the separation regions (darkest blue zones) behind the roughness element which start from the separation point and end with the node point of attachment where all the skin friction lines are directed outward away from the node. In Fig. 13(b) there is also evidence of a second smaller separation region before the hump. The separation regions and the difference of their extension are more evident in Fig. 14, which shows the pressure distribution over the same humps, 11.70% and 23.40% in a plane along the centerline of the domain.

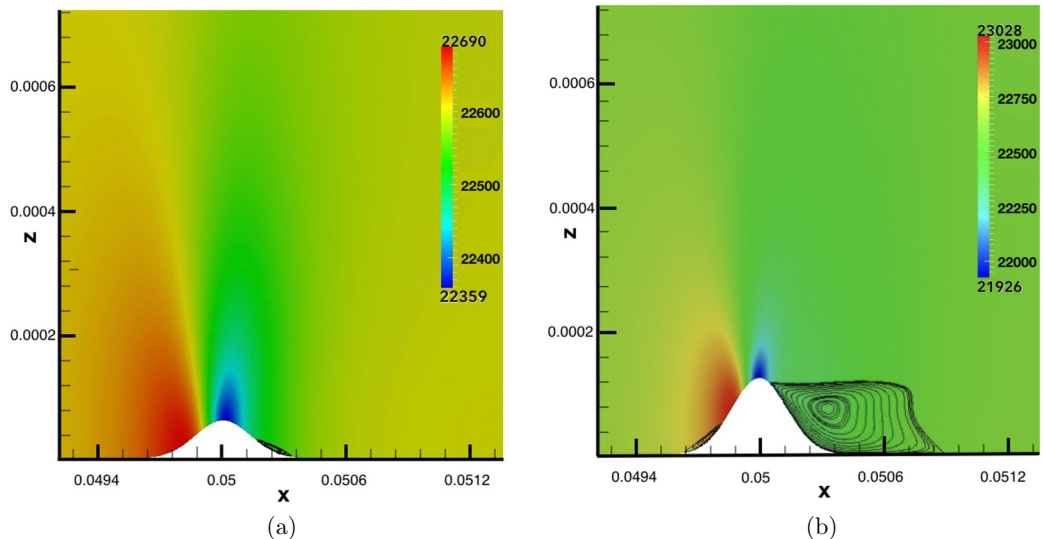


FIG. 14. Pressure distribution and recirculation regions on a plane along the centerline of the domain, varying the hump heights: (a) 11.70% and (b) 23.40%.

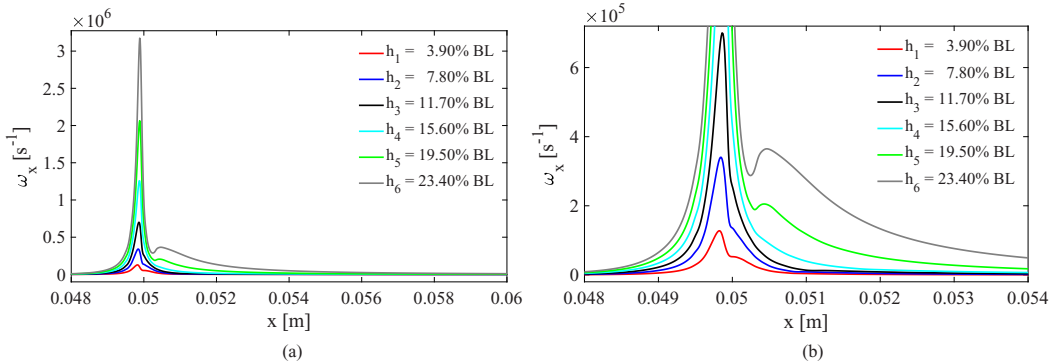


FIG. 15. Magnitude of maximum streamwise vorticity. (b) Close-up around the hump location in (a).

It is possible to appreciate that the disturbance generated by the hump in Fig. 14(b) is much bigger than that in Fig. 14(a) in terms of both pressure and separation bubbles. We also note the unusual shape of the separation bubble for the 23.40% hump that is caused by the streamwise vortices forming downstream of the hump.

#### D. Streamwise vortices

In this section we analyze the generation of streamwise vortices caused by the different humps. The existence of these vortices is the main difference between the flow with a two-dimensional and a three-dimensional hump. In fact, streamwise vortices are created only by three-dimensional roughness elements. The main feature of the flow considered is the wake behind the roughness, which is composed of two symmetric counterrotating vortices.

Figure 15 shows the maximum value of the streamwise vorticity at different locations in the streamwise direction. Specifically, we extracted the streamwise vorticity distribution at different planes and we identified its maximum value and the correspondent  $(x, z)$  location for each plane. We can see that the distortion increases as the height of the roughness increases. The maximum value is in proximity to the hump location. After the maximum the streamwise vorticity starts to decrease monotonically for the 3.90%, 7.80%, 11.70%, and 15.60% humps, rapidly approaching the unperturbed value. As already seen for the pressure and shear stress, the vorticity of the 19.50% and 23.40% humps is different and this is evident in Fig. 15(b). The streamwise vorticity reaches a minimum inside the separation region; after this minimum it starts to slightly increase. We then observe a second maximum in the separation region and after this the vorticity decreases monotonically, returning to the unperturbed value. Figure 16 shows the location of the streamwise vortices in the wall-normal direction  $z$  at different values of  $x$ . In particular, we see that the generation of streamwise vortices appears evident from the 19.50% hump and the length of these vortices downstream of the roughness increases with the hump height. Considering the height hump as the reference length, the streamwise vortices of the 19.50% and 23.40% humps extend for different lengths after the hump location. We see that the vortices grow in length downstream of the hump and move away from the wall. The vertical motion of the vortices can be explained by their rotation visible from the streamlines of Fig. 17, which shows the streamwise vorticity and the pressure of the 19.50% hump in a plane perpendicular to the streamwise velocity at  $x = x_h + 4h$ ,  $x_h$  being the location of the hump center and  $h$  the hump height. Specifically, observing the in-plane streamlines, we can see that the rotation of each vortex induces a positive vertical motion on the other and this results in a central upwash. As seen in [46], the sense of rotation of the vortices depends on both the shape of the obstacle and its depth relative to the boundary-layer height. Obstacles that divide the stream

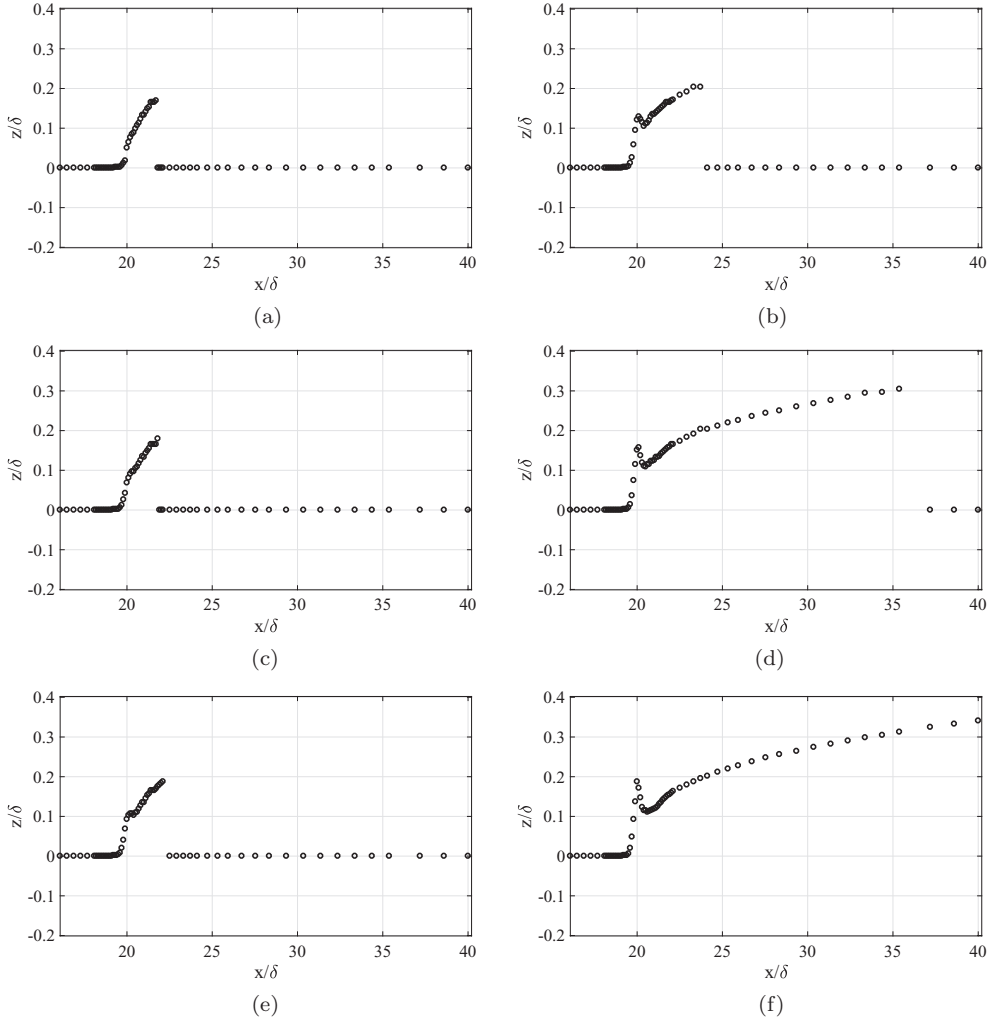


FIG. 16. The  $Z$  location of maximum streamwise vorticity for the different hump heights: (a) 3.90%, (b) 15.60%, (c) 7.80%, (d) 19.50%, (e) 11.70% and (f) 23.40%.

laterally produce vortices with a central downwash, whereas those lifting the flow predominantly over their crests, such as the humps considered in this study, produce vortices with a central upwash. In particular, the direction of the streamlines can be explained through the pressure distribution. In this plane, inside the separation bubble and close to the center of the hump the pressure away from the symmetry plane is larger than the pressure in the region close to this. This causes a motion of the flow towards the plane  $y = 0$ , as we can see in the bottom part of Fig. 17.

When the flow approaches the symmetry plane from both the left and the right there is a collision of the fluid particles which causes a positive wall-normal velocity. The flow motion in the plane  $y = 0$  is towards the top of the domain, but the pressure in the upper part of the domain increases and is close to the unperturbed value. This results in a change in the flow direction visible from the streamlines that start to diverge towards negative and positive values of  $y$ . The separation characterized by the collision of the flow in the symmetry plane results in this typical mushroom-shaped plume that we can well appreciate in the streamlines of Fig. 17.

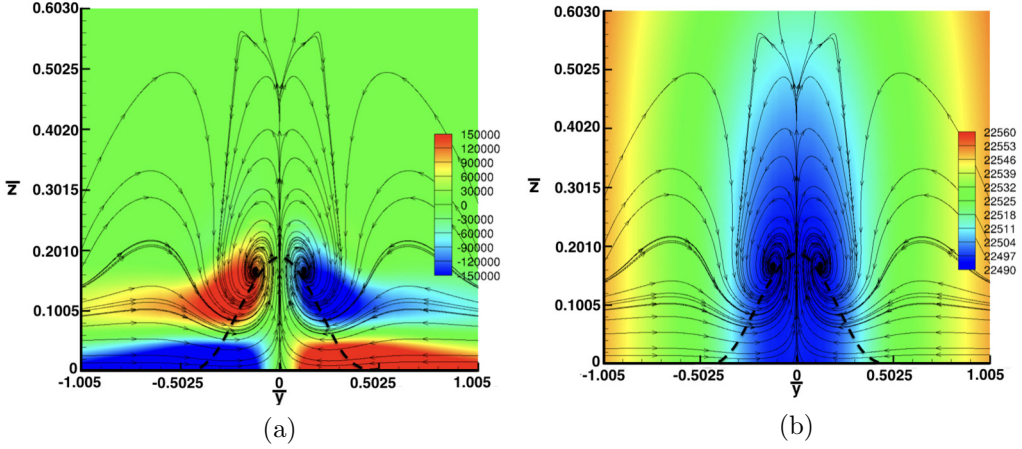


FIG. 17. (a) Streamwise vorticity and (b) pressure for the 19.50% hump at  $x = x_{hump} + 4h_r$  after the hump location.

## V. SUMMARY

In this paper the DNS results of a two-dimensional boundary-layer flow encountering a three-dimensional Gaussian-shaped roughness element were presented. The flow outside of the boundary layer is a high-speed subsonic flow at  $\text{Ma} = 0.87$ . The Reynolds number considered based on the distance from the leading edge of the flat plate is  $\text{Re} = 4 \times 10^5$  and is sufficiently high to be considered in the regime of aeronautical applications.

We first showed a comparison between the results of a three-dimensional hump and of an identically shaped two-dimensional hump in terms of  $dp/dx$  and  $\tau_{xz}$ . From the calculation it is possible to appreciate that the perturbations produced by the two-dimensional humps are bigger than those produced by the equivalent three-dimensional humps, in terms of both peaks and extension. This can be explained by the smaller blockage effect generated by the three-dimensional roughness elements.

We then studied the effect that the Mach number can have on a similar flow comparing the transonic regime of  $\text{Ma} = 0.87$  with a subsonic of  $\text{Ma} = 0.5$ . The results obtained for the normalized  $dp/dx$  and  $\tau_{xz}$  show very similar qualitative distributions of the quantities considered, in terms of extension of the distortion, hump height at which the separation first occurs, and location of the separation point. The separation behind the hump seems to appear at similar hump heights and the extension of the separation zone is the same. After these numerical comparisons we focused on the transonic regime  $\text{Ma} = 0.87$  and we studied different hump heights. Specifically, we found, as expected, that the distortion of the boundary layer increases with the increase in roughness height. After a critical hump height we start to see a separation zone downstream of the roughness whose extension becomes larger with larger values of the height. With a further increase of the hump height, a separation zone begins to develop upstream of the roughness as well. In addition, the calculations show that when the roughness height is sufficiently large, two counterrotating vortices form in the wake behind the roughness. They move slowly away from the wall and extend for different hump lengths after the roughness location with their longitudinal size increasing with the height of the hump. The pressure perturbations instead decay rather fast and this suggests that the pressure is unlikely to play a decisive role in supporting the presence of the vortices even far from the hump, as already predicted by the asymptotic analysis performed in [17].

This work constitutes a step to close the gap between the DNS results in high-speed subsonic regimes and the data present in the literature for similar analyses in supersonic and hypersonic regimes.

### ACKNOWLEDGMENTS

This work was supported by the Laminar Flow Control Centre funded by Airbus/EADS and EPSRC under Grant No. EP/I037946 and computational resources were also provided through the UK Turbulence resource under EPSRC Grant No. EP/L000261/1. The authors would like to acknowledge the use of Imperial College High Performance Computing facility. S.J.S. would also like to acknowledge support under the RAEng Fellowship through Grant No. 10145/86.

---

- [1] L. Prandtl, Über Flüssigkeitsbewegung bei sehr kleiner Reibung, Verh. III, Intern. Math. Kongr. Heidelberg, Auch: Gesammelte Abhandlungen **2**, 484 (1904).
- [2] V. Y. Neiland, Theory of separation of a laminar boundary layer in a supersonic stream, Izv. Akad. Nauk SSSR, Mekh. Zhidk. Gaza **4**, 53 (1969).
- [3] K. Stewartson and P. G. Williams, Self-induced separation, *Proc. R. Soc. London Ser. A* **312**, 181 (1969).
- [4] K. Stewartson, On the flow near the trailing edge of a flat plate II, *Mathematika* **16**, 106 (1969).
- [5] A. F. Messiter, Boundary-layer flow near the trailing edge of a flat plate, *SIAM J. Appl. Math.* **18**, 241 (1970).
- [6] V. V. Sychev, A. I. Ruban, and G. L. Korolev, *Asymptotic Theory of Separated Flows* (Cambridge University Press, Cambridge, 1998).
- [7] F. T. Smith, R. I. Sykes, and P. W. Brighton, A two-dimensional boundary layer encountering a three-dimensional hump, *J. Fluid Mech.* **83**, 163 (1977).
- [8] R. I. Sykes, Stratification effects in boundary layer flows over hills, *Proc. R. Soc. London Ser. A* **361**, 225 (1978).
- [9] F. T. Smith, Pipeflows distorted by non-symmetric indentation or branching, *Mathematika* **23**, 62 (1976).
- [10] F. Smith, A three-dimensional boundary layer separation, *J. Fluid Mech.* **99**, 185 (1980).
- [11] R. I. Sykes, On three-dimensional boundary layer flows over surface irregularities, *Proc. R. Soc. London Ser. A* **373**, 311 (1980).
- [12] V. V. Bogolepov and V. Y. Neiland, Supersonic flow over a surface with local distortions, TsAGI Trans. **1363**, 1 (1971).
- [13] V. V. Bogolepov and V. Y. Neiland, Locally three-dimensional boundary flows, *Tekh. Fiz.* **1**, 28 (1985).
- [14] G. L. Korolev, Method for solving the equations describing the interaction of a three-dimensional boundary layer with an outer inviscid flow, *Comput. Math. Math. Phys.* **47**, 487 (2007).
- [15] M. E. Goldstein, A. Sescu, P. W. Duck, and M. Choudhari, The long range persistence of wakes behind arrow of roughness elements, *J. Fluid Mech.* **644**, 123 (2010).
- [16] M. E. Goldstein, A. Sescu, P. W. Duck, and M. Choudhari, Algebraic/transcendental disturbance growth behind a row of roughness elements, *J. Fluid Mech.* **668**, 236 (2011).
- [17] A. I. Ruban and M. A. Kravtsova, Generation of steady longitudinal vortices in hypersonic boundary layer, *J. Fluid Mech.* **729**, 702 (2013).
- [18] O. Marxen and G. Iaccarino, Numerical simulation of the effect of a roughness element on high-speed boundary-layer instability, *Proceedings of the 38th Fluid Dynamics Conference* (AIAA, Seattle, 2008), AIAA paper 2008-4400.
- [19] G. Groskopf, M. J. Kloker, and O. Marxen, *Bi-Global Secondary Stability Theory for High-Speed Boundary-Layer Flows*, Center for Turbulence Research, Proceedings of the Summer Program (Stanford University, Stanford, 2008).
- [20] M. Choudhari, F. Li, M. Wu, C. L. Chang, J. Edwards, M. Kegerise, and R. King, Laminar-turbulent transition behind discrete roughness elements in a high-speed boundary layer, *Proceedings of the 48th AIAA Aerospace Sciences Meeting* (AIAA, Orlando, 2010), AIAA Paper 2010-1575.
- [21] M. Choudhari, A. Norris, F. Li, C. L. Chang, and J. Edwards, Wake instabilities behind discrete roughness elements in high speed boundary layers, *Proceedings of the 51st AIAA Aerospace Sciences Meeting including the New Horizons Forum and Aerospace Exposition* (AIAA, Texas, 2013), AIAA Paper 2013-0081.

- [22] J. A. Redford, N. D. Sandham, and G. T. Roberts, Compressibility effects on boundary-layer transition induced by an isolated roughness element, *AIAA J.* **48**, 2018 (2010).
- [23] M. Bernardini, S. Pirozzoli, and P. Orlandi, Compressibility effects on roughness-induced boundary layer transition, *Int. J. Heat Fluid Flow* **35**, 45 (2012).
- [24] M. Bernardini, S. Pirozzoli, P. Orlandi, and S. K. Lele, Parameterisation of boundary-layer transition induced by isolated roughness elements, *AIAA J.* **52**, 2261 (2014).
- [25] N. De Tullio and N. D. Sandham, Direct numerical simulations of roughness receptivity and transitional shock-wave/boundary-layer interactions, NATO Report No. RTO-MP-AVT-200, 2012 (unpublished).
- [26] N. De Tullio and N. D. Sandham, Influence of boundary-layer disturbances on the instability of a roughness wake in a high-speed boundary layer, *J. Fluid Mech.* **763**, 136 (2015).
- [27] N. De Tullio, P. Paredes, N. D. Sandham, and V. Theofilis, Laminar-turbulent transition induced by a discrete roughness element in a supersonic boundary layer, *J. Fluid Mech.* **735**, 613 (2013).
- [28] J. Van den Eynde, Stability and transition of the flow behind isolated roughness elements in hypersonic boundary layers, Ph.D. thesis, University of Southampton, 2015.
- [29] S. P. Schneider, Effects of roughness on hypersonic boundary-layer transition, *J. Spacecr. Rockets* **45**, 193 (2008).
- [30] B. M. Wheaton, M. D. Bartkovicz, P. K. Subbareddy, S. P. Schneider, and G. V. Candler, *Proceedings of the 41st AIAA Fluid Dynamics Conference and Exhibit* (AIAA, Reston, 2011), paper 2011-3248.
- [31] G. Mengaldo, M. Kravtsova, A. I. Ruban, and S. J. Sherwin, Triple-deck and direct numerical simulation analyses of high-speed subsonic flow over a roughness element, *J. Fluid Mech.* **774**, 311 (2015).
- [32] G. Mengaldo, Discontinuous spectral/hp element methods: development, analysis and applications to compressible flows, Ph.D. thesis, Imperial College London, 2015.
- [33] C. D. Cantwell, D. Moxey, A. Comerford, A. Bolis, G. Rocco, G. Mengaldo, D. De Grazia, S. Yakolev, J.-E. Lombard, D. Ekelshot *et al.*, Nektar++: An open-source spectral/hp element framework, *Comput. Phys. Commun.* **192**, 205 (2015).
- [34] D. De Grazia, High order spectral/hp element methods for compressible boundary layers on hexahedral grids, Ph.D. thesis, Imperial College London, 2016.
- [35] D. A. Kopriva, S. L. Woodruff, and M. Y. Hussaini, Discontinuous spectral element approximation of maxwells equations, in *Discontinuous Galerkin Methods*, edited by B. Cockburn, G. E. Karniadakis, and C.-W. Shu, Lecture Notes in Computational Sciences and Engineering, Vol. 11 (Springer, Berlin, 2000).
- [36] D. A. Kopriva and G. Gassner, On the quadrature and weak form choices in collocation type discontinuous Galerkin spectral element methods, *J. Sci. Comput.* **44**, 136 (2010).
- [37] J. S. Hesthaven and T. Warburton, *Nodal Discontinuous Galerkin Methods—Algorithms, Analysis, and Applications* (Springer, Berlin, 2008).
- [38] E. F. Toro, *Riemann Solvers and Numerical Methods for Fluid Dynamics*, 3rd ed. (Springer, Berlin, 2009).
- [39] G. Mengaldo, D. De Grazia, J. Peiro, A. Farrington, F. Witherden, P. E. Vincent, and S. J. Sherwin, *Proceedings of the 7th AIAA Theoretical Fluid Mechanics Conference* (AIAA, Reston, 2014).
- [40] B. Cockburn and C.-W. Shu, The local discontinuous Galerkin method for time-dependent convection-diffusion systems, *SIAM J. Numer. Anal.* **35**, 2440 (1998).
- [41] D. Moxey, M. Hazan, S. J. Sherwin, and J. Peiro, An isoparametric approach to high-order curvilinear boundary-layer meshing, *Comput. Methods Appl. Mech. Eng.* **283**, 636 (2015).
- [42] G. Mengaldo, D. De Grazia, D. Moxey, P. E. Vincent, and S. J. Sherwin, Dealiasing techniques for high-order spectral element methods on regular and irregular grids, *J. Comput. Phys.* **299**, 56 (2015).
- [43] F. M. White, *Viscous Fluid Flow*, 3rd ed. (McGraw-Hill, New York, 2006).
- [44] B. Wasistho, Spatial direct numerical simulation of compressible boundary layer flow, Ph.D. thesis, University of Twente, 1997.
- [45] G. L. Korolev, J. S. B. Gajjar, and A. I Ruban, Once again on the supersonic flow separation near a corner, *J. Fluid Mech.* **463**, 173 (2002).
- [46] P. J. Mason and B. R. Morton, Trailing vortices in the wakes of surface-mounted obstacles, *J. Comput. Phys.* **175**, 247 (1987).